


Coherent Pulse Echo in Hybrid Magnonics with Multimode Phonons

Jing Xu,¹ Changchun Zhong^{1,2}, Xianjing Zhou¹, Xu Han,¹ Dafei Jin,¹ Stephen K. Gray¹,
Liang Jiang² and Xufeng Zhang^{1,*}

¹*Center for Nanoscale Materials, Argonne National Laboratory, Lemont, Illinois 60439, USA*

²*Pritzker School of Molecular Engineering, University of Chicago, Chicago, Illinois 60637, USA*

 (Received 14 April 2021; revised 20 June 2021; accepted 20 July 2021; published 5 August 2021)

The hybridization of magnons and phonons is playing a critical role in the emerging field of hybrid magnonics because it combines the high tunability of magnetism with the long lifetime of mechanics for comprehensive coherent information processing. Recently there has been increasing interest in thin-film bulk acoustic waves because of their long lifetimes at high frequencies. However, the unique multimode nature of such phonon modes has not been exploited as an important resource for coherent information processing. In this Letter we study the simultaneous hybridization of multiple high-overtone bulk acoustic resonances with a magnon and a microwave mode. The demonstrated multimode hybridization allows us to observe coherent pulse echoes, opening opportunities for both fundamental studies and practical applications of hybrid magnonics.

DOI: [10.1103/PhysRevApplied.16.024009](https://doi.org/10.1103/PhysRevApplied.16.024009)

Hybrid magnonics has been undergoing rapid developments in the past few years. With a focus on studying the coherent interactions between magnons—quantized collective spin excitations known as spin waves—and other degrees of freedom such as electromagnetic waves, hybrid magnonics enables coherent information exchange among different physical platforms and therefore is of great importance for both fundamental research and practical applications [1–9]. For instance, the coherent interaction between magnons and cavity microwave photons can far exceed their dissipation rates because the interaction can be significantly enhanced by the large spin density of magnetic materials such as yttrium iron garnet (YIG) [1–5]. Such strong coupling has been widely studied in different device configurations, opening a broad variety of applications ranging from nonreciprocal signal routing [10–12], non-Hermitian physics [13–15], and microwave-to-optical transduction [16,17] to dark matter detection [18,19] and quantum magnonics [20–22].

Among various excitations that can hybridize with magnons, mechanical phonons are of particular interest because of their unique properties such as long lifetime and compact footprint [23–26]. The interaction between magnons and phonons has been employed for decades in classical signal processing [27–43]. With the recent development of hybrid magnonics for coherent or even quantum information processing, there is renewed interest in hybridizing magnons and phonons [9]. Recent

experimental and theoretical demonstrations of phonon-magnon coupling on macroscopic YIG sphere devices have revealed its great potential for functionalities including ground-state cooling [44], magnon-phonon entanglement [45], nonreciprocal phonon propagation [46,47], etc. However, these spherical phonon modes are limited by their low resonance frequencies (typically in the megahertz range), which are not favorable for future quantum applications because of the extremely low temperature required to suppress the thermal noise.

High-overtone bulk acoustic wave resonances (HBARs) represent another type of phonon mode supported by thin-film YIG devices [48–51]. With frequencies covering the gigahertz range, they can directly couple with magnon resonances through the magnetoelastic effect [52]. One distinct feature of HBARs is that multiple evenly distributed resonances can be supported on a single resonator, but this multimode nature has been rarely explored so far. In this Letter, we show that by hybridizing a magnon resonance, a microwave resonance, and multiple HBAR phonon modes, coherent pulse echoes can be observed on a YIG thin-film device. Such a configuration takes advantage of not only the multimode nature of the phonon modes but also their long lifetimes, enabling more functionalities for magnon-based coherent information processing.

Figure 1(a) shows the schematics of our planar device that simultaneously supports microwave, magnon, and HBAR phonon resonances. A rectangular splitting resonator (RSRR) is fabricated together with a coupling microstrip on a printed circuit board (model TMM10i [53]). It supports a microwave resonance

*Corresponding author. xufeng.zhang@anl.gov

[Fig. 1(b)] at frequency $\omega_a = 2\pi \times 9.32$ GHz (with the YIG chip loaded). The compact RSRR design ensures a highly focused distribution of the microwave field, which enhances the coupling between microwave photons and magnons in the YIG film.

A magnonic device is placed atop the RSRR with the YIG side facing down. The 200-nm-thick epitaxial YIG film is patterned into a 0.8×0.9 mm² rectangle on a 527- μ m-thick single-crystal gadolinium gallium garnet (GGG) [111]-oriented substrate. A bias magnetic field is applied by a permanent magnet along the out-of-plane (z) direction to support forward volume magnetostatic wave magnons, whose dynamic magnetization $m(t) = [m_x(z) + im_y(z)]e^{-i\omega_m t}$ rotates in the x - y plane with m_x (m_y) being the x (y) component [54]. The resonance frequency of the fundamental magnon mode can be approximated as $\omega_m = \gamma\sqrt{H(H + M_s)}$, where $\gamma = 2\pi \times 28$ GHz/T is the gyromagnetic ratio and $M_s = 0.175$ T is the saturation magnetization of YIG. The bias field H can be tuned by moving the magnet position (z) to sweep the magnon frequency.

In addition to magnon resonances, our device also supports HBAR phonons. Transverse elastic waves can propagate along the thickness (z) direction and form high-order standing waves between the top and bottom surfaces of the YIG/GGG structure [Fig. 1(c)]. Because of the similar mechanical properties of YIG and GGG, the standing waves are distributed across both layers along the

thickness direction. In the lateral direction, the phonon modes are confined by the YIG boundaries, as indicated by our COMSOL simulation results in Fig. 1(d) (magnon-phonon interaction not considered). Considering the large wavelength in the lateral direction, uniform lateral phonon distribution can be assumed for simplicity. The displacement of transverse phonons [54] is mainly in plane $u_{in} = [u_x(z) + iu_y(z)]e^{-i\omega_{bn}t}$, where u_x (u_y) is the x (y) displacement and ω_{bn} is the frequency of the n th-order mode, while their z displacement can be neglected. From the simulated spectrum [Fig. 1(e)], multiple phonon resonances can be observed, with an even spacing of 3.40 MHz. This agrees with the theoretical calculation of the free spectral range (FSR) $\Delta f = c_s/2d = 3.32$ MHz, where d is the chip thickness and $c_s = \sqrt{E/[2(1 + \nu)\rho]}$ is the propagation speed of transverse elastic waves (E is Young's modulus, ν is Poisson's ratio, and ρ is the density). All parameters used here are for GGG (Table I), while the YIG layer is ignored in calculation because of its ultrasmall thickness and similar mechanical properties.

Under the rotating wave approximation, our system can be described by the Hamiltonian

$$\hat{H} = \hbar\Delta_a\hat{a}^\dagger\hat{a} + \hbar\Delta_m\hat{m}^\dagger\hat{m} + \hbar\sum_n\Delta_{bn}\hat{b}_n^\dagger\hat{b}_n + \hbar\sqrt{\kappa_0}E_{in}(\hat{a} - \hat{a}^\dagger) + \hat{H}_{int}, \quad (1)$$

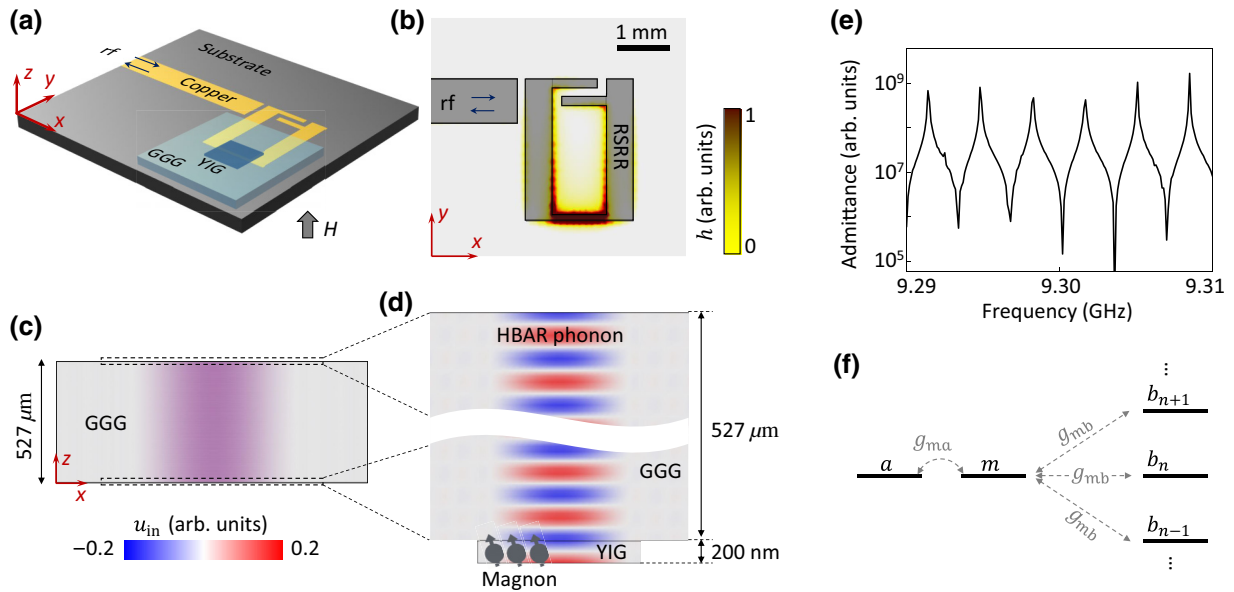


FIG. 1. (a) Device schematics showing a YIG/GGG chip flipped (YIG side facing down) atop a copper RSRR. The device has a single input and output port for reflection measurements. A bias magnetic field H is applied along the z direction. (b) Simulated microwave magnetic field h distribution of the RSRR resonance, with the field localized around the short inductor wire. (c) Simulated in-plane displacement (u_{in}) of the transverse HBAR in the YIG/GGG chip. (d) Enlargement of the phonon in-plane displacement, which is distributed across the whole chip thickness and laterally confined by the YIG boundaries. Spatial overlap of HBAR phonons with magnons in YIG is also indicated. (e) Simulated HBAR spectrum, revealing the evenly distributed multimodes. (f) Energy level diagram of our photon-magnon-phonon hybrid system.

TABLE I. Mechanical properties of YIG and GGG.

	Young's modulus E (Pa)	Poisson's ratio ν	Density ρ (kg/m ³)	Thickness d (μm)
YIG [55]	0.2×10^{12}	0.29	5170	0.2
GGG [56]	0.222×10^{12}	0.28	7080	527

where \hat{a}^\dagger (\hat{a}), \hat{m}^\dagger (\hat{m}), and \hat{b}_n^\dagger (\hat{b}_n) are the creation (annihilation) operators of the microwave photon, the magnon, and the n th overtone phonon mode, respectively. In addition, κ_0 is the cavity external coupling rate and $E_{\text{in}} = \sqrt{P/\hbar\omega_0}$ is the time-dependent input field with P and ω_0 being its power and frequency, respectively. The detunings of the three modes are given as $\Delta_a = \omega_a - \omega_0$, $\Delta_m = \omega_m - \omega_0$, and $\Delta_{bn} = \omega_{bn} - \omega_0$, respectively. In our experiments, we have on-resonance condition $\Delta_a = \Delta_m = 0$.

The interaction term of the Hamiltonian is

$$\hat{H}_{\text{int}} = \hbar g_{ma} (\hat{m}^\dagger \hat{a} + \hat{m} \hat{a}^\dagger) + \hbar \sum_n g_{mb} (\hat{m}^\dagger \hat{b}_n + \hat{m} \hat{b}_n^\dagger), \quad (2)$$

as illustrated by Fig. 1(f), where g_{ma} (g_{mb}) is the coupling strength between magnon and photon (phonon) modes. In addition to the widely studied magnon-photon coupling, coexisting phonons and magnons in YIG interact with each other via the magnetoelastic effect [57]:

$$U_{\text{ME}} = \frac{B_2}{M_s} \left(m_x \frac{\partial u_x}{\partial z} + m_y \frac{\partial u_y}{\partial z} \right), \quad (3)$$

where U_{ME} represents the magnetoelastic energy density (only the dominant first-order effects are considered) and B_2 is the magnetoelastic constant of YIG. Accordingly, the magnon-phonon coupling strength $g_{mb} \propto \int U_{\text{ME}} dV$ can be optimized by maximizing the integral over the device volume V . Assuming a uniform magnon distribution along the thickness direction [58], an optimal coupling can be obtained when the phonon wavelength $\lambda/2 = d_{\text{YIG}} = 0.2 \mu\text{m}$. Using the transverse phonon speed in YIG, $c'_s = 3910 \text{ m/s}$, an optimal operation frequency $\omega = 2\pi c'_s/\lambda = 2\pi \times 9.8 \text{ GHz}$ is obtained, approximately corresponding to the 2960th overtone phonon resonance. Our measurements are taken within a small span around this frequency, and therefore the coupling strengths for all phonon modes are considered identical. Although the phonon modes occupy the whole YIG/GGG thickness, they only interact with magnons in the thin YIG layer. The small mode overlap limits the obtainable magnon-phonon coupling strength. But as is shown below, the coupling can still exceed the extremely low phonon dissipation in GGG.

The photon-magnon-phonon interaction is studied by measuring RSRR reflections around ω_a using a vector network analyzer (VNA), considering that the optimal magnon-phonon coupling frequency is near the RSRR

resonance. Figure 2(a) plots the typical spectra of the device reflection when a continuous-wave microwave tone is sent to the device, revealing an anticrossing feature as the magnon mode is swept across the RSRR resonance. Numerical fitting gives a coupling strength $g_{ma} = 2\pi \times 23 \text{ MHz}$, which is less than the microwave dissipation rate $\kappa_a/2 = 2\pi \times 59 \text{ MHz}$ but exceeds the magnon dissipation $\kappa_m/2 = 2\pi \times 1.2 \text{ MHz}$, leading to a cooperativity $C = 4g_{ma}^2/\kappa_a\kappa_m = 7.5$.

Additional anticrossing features can be observed from the enlarged spectra at low VNA powers [Fig. 2(a), inset], corresponding to the coupling between HBAR phonon and magnon modes. Numerical fitting shows that the magnon-phonon coupling is $g_{mb} = 2\pi \times 0.75 \text{ MHz}$, smaller than the magnon dissipation but larger than the extracted phonon dissipation $\kappa_b/2 = 2\pi \times 0.3 \text{ MHz}$, resulting in a cooperativity $C = 4g_{mb}^2/\kappa_m\kappa_b = 1.6$. At elevated VNA powers, the phonon features become more prominent, as indicated by the fine horizontal lines in Figs. 2(b) and 2(c). In fact, the magnon resonance exhibits a foldover [59,60] because of the intrinsic magnon nonlinearity, causing the magnon frequency to shift towards higher frequencies when swept at high VNA powers [Figs. 2(d) and 2(e)]. Therefore, the magnon-phonon coupling can be read out in a broader frequency range. These spectra give a phonon FSR of $\Delta f = 3.31 \text{ MHz}$, which agrees well with theoretical and simulation results.

Spectral analysis shows that our triply resonant system resembles atomic frequency combs [61,62]. Such an effect is absent when the magnon is tuned off-resonance from the microwave resonance, where only a single phonon mode can be read out near the narrow magnon resonance. When the magnon is hybridized with the large-linewidth photon mode, the resulting hybrid modes interact more efficiently with, and hence read out, phonons in a broader frequency range, exhibiting a comblike spectrum, which leads to pulse echoes when excited by a microwave pulse. The temporal response of our system can be described by the Heisenberg-Langevin equations (in the matrix form):

$$\dot{\mathbf{v}} = \mathbf{M} \cdot \mathbf{v} + \mathbf{v}_{\text{in}}, \quad (4)$$

where vector $\mathbf{v} = \{a, m, b_1, b_2, \dots, b_n, \dots\}^T$ collects all the system modes, $\mathbf{v}_{\text{in}} = \{\sqrt{\kappa_0}E_{\text{in}}, 0, 0, 0, \dots\}^T$ describes the input modes, and \mathbf{M} is the dynamical matrix

$$\mathbf{M} = \begin{pmatrix} -\kappa_a/2 & ig_{ma} & 0 & 0 & & \\ ig_{ma} & -\kappa_m/2 & ig_{mb} & ig_{mb} & \dots & \\ 0 & ig_{mb} & i\Delta_{b1} - \kappa_b/2 & 0 & & \\ 0 & ig_{mb} & 0 & i\Delta_{b2} - \kappa_b/2 & & \\ & \vdots & & & \ddots & \end{pmatrix}. \quad (5)$$

Since our system operates in the classical regime, the hats on the operators can be dropped to represent their

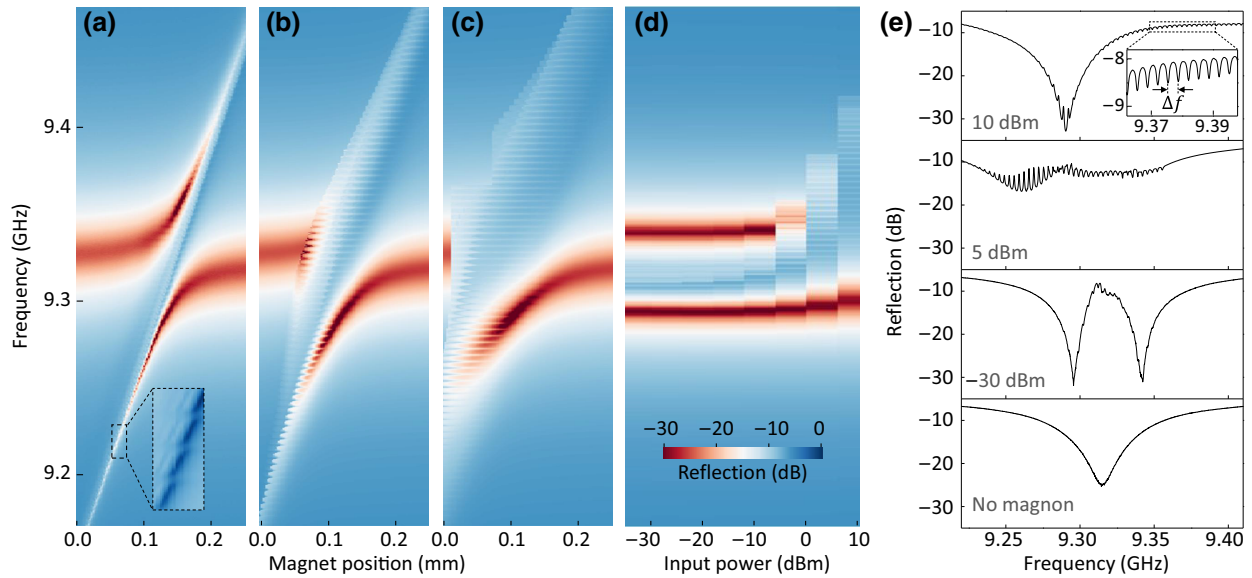


FIG. 2. Measured microwave reflection spectra of the RSRR with VNA powers of (a) -30 dBm, (b) 0 dBm, and (c) 5 dBm as the magnon frequency is swept by the magnet position. Inset: enlarged magnon-phonon anticrossing feature when the magnon is off-resonance from the RSRR resonance. (d) Measured RSRR reflection spectra for a fixed magnon frequency (initially on-resonance with the RSRR) versus the VNA power. (e) Line plots for different VNA powers. Pure RSRR resonance is observed when there is no magnon. The magnon-photon normal-mode splitting appears at -30 dBm, smears out at 5 dBm, and disappears at 10 dBm. Phonon features become more prominent at 5 and 10 dBm, revealing a phonon FSR of $\Delta f = 3.31$ MHz.

classical average values. The system dynamics can be solved as

$$\mathbf{v}(t) = \mathbf{Z}(t)\mathbf{C} + \mathbf{Z}(t) \int_0^t \mathbf{Z}^{-1}(\tau)\mathbf{v}_{in}d\tau, \quad (6)$$

where \mathbf{C} is a constant column vector determined by the initial condition, $\mathbf{Z}(t) = \mathbf{U}e^{\mathbf{D}t}$ with \mathbf{U} representing a unitary transform that diagonalizes the dynamical matrix, $\mathbf{D} = \mathbf{U}\mathbf{M}\mathbf{U}^{-1}$.

To measure the pulse echo, a microwave pulse centered at ω_0 with a -10 -dBm peak power, which is obtained by mixing a microwave tone with a triangular pulse (12 ns for the rise and fall edges each), is sent to the RSRR [Fig. 3(a)]. Fourier transform shows that such a microwave pulse has a full width at half maximum of 74 MHz, covering around 23 HBAR phonon modes [Fig. 3(b)]. The reflection signal, separated from the input signal by a circulator to avoid unnecessary interference, is sent to a high-speed sampling oscilloscope to monitor the device response. The pulsed measurements are repeated with a repetition time of $2 \mu\text{s}$.

Figure 4(a) plots the measured pulse echo process. Following the microwave pulse input at time $t = 0$, the microwave signal is coupled to multiple phonon modes through a magnon-mediated process. After the phonon modes become populated, they start to dephase because of the frequency difference among HBAR modes, leading to the disappearance of the pulse. After evolving for $t = 304$ ns, all the phonon modes become in phase again,

generating a sharp echo pulse at the RSRR output via another magnon-mediated process. Second and third echo pulses are also observed at around $t = 605$ and 902 ns, respectively, because of the long lifetime of the HBAR phonons. Coherent pulse echoes can be observed when the magnon frequency is tuned in a broad range by varying the bias magnet position.

The measured device dynamics qualitatively matches the theoretical calculation with 18 phonon modes [Fig. 4(b)], with the observed echo period agreeing with theory prediction: $\delta t = 1/\Delta f = 303$ ns. The additional fringes on

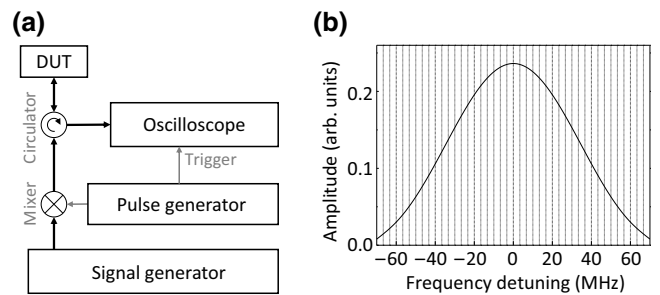


FIG. 3. (a) Setup configuration for time-domain characterization. The signal generator and pulse generator outputs are mixed by the mixer to produce the input microwave pulse. The device reflection is separated from the input by a circulator and recorded by an oscilloscope. DUT: device under test. (b) Fourier transform of the input triangular pulse versus frequency detuning. Dashed vertical lines indicate phonon resonance frequencies.

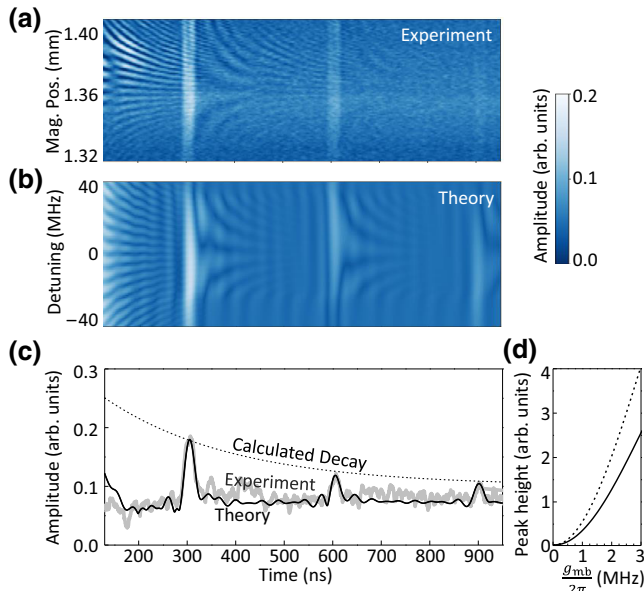


FIG. 4. Measured (a) and calculated (b) amplitude of the cavity reflection as a function of time at various magnon detunings $\Delta_{ma} = \omega_m - \omega_a$ after a triangular pulse input at $t = 0$, showing three echo pulses at 304, 605, and 902 ns. The detuning is controlled by the magnet position [Mag. Pos. in (a)]. (c) Line plot comparison of the measured (thick gray line) and calculated (solid black line) echo signal for zero magnon detuning ($\Delta_{ma} = 0$). Dashed black line: calculated exponential echo decay caused by phonon dissipation. (d) Calculated height of the first echo peak versus the magnon-phonon coupling strength $g_{mb}/2\pi$ for two different phonon dissipation rates: $\kappa_b = 2\pi \times 0.55$ MHz (solid line) and $\kappa_b = 2\pi \times 0.055$ MHz (dashed line).

the spectra can be attributed to interferences with crosstalk and additional high-order magnon modes, which is confirmed by the numerical simulation and suppressing these noises is beyond the scope of this work. This storage mechanism utilizes the multimode nature of the phonon modes, and therefore can be extended to the echo of multiple input pulses [63].

Figure 4(c) shows that in addition to the period, the relative amplitudes of the echo pulses also match the theoretical prediction based on the measured phonon dissipation κ_b [dashed line in Fig. 4(c)]. Further enhancement of the echo can be expected through improved design and characterization approaches. For instance, stronger echo peaks can be obtained by increasing the magnon-phonon coupling strength [Fig. 4(d)]. This can be achieved by improving the magnon-phonon mode overlap using a substrate with a thicker YIG layer or thinner GGG layer. Alternatively, reduced phonon linewidths also help improve the echo peak height, which can be realized via cryogenic operations or comprehensive device engineering.

In summary, we experimentally observe the coherent coupling between microwave photons, magnons, and multimode HBAR phonons, and demonstrate coherent pulse

echoes on the hybrid photon-magnon-phonon system. We have also developed a complete theory for modeling the Hamiltonian and dynamics of our system. Currently our device performance is limited by the finite magnon-phonon coupling rate and the finite phonon lifetime. Since our phonon lifetime is much longer than both the magnon and photon modes, our demonstration can potentially be extended to develop multimode memories for magnons. Most importantly, our work utilizes the multimode nature of HBAR phonons as an important resource for magnon-based coherent information processing, opening opportunities for a broad range of applications including quantum magnonics.

ACKNOWLEDGMENTS

This material is based upon the work supported by Laboratory Directed Research and Development (LDRD) funding from the Argonne National Laboratory, provided by the Director, Office of Science, of the U.S. Department of Energy under Contract No. DE-AC02-06CH11357. The use of the Center for Nanoscale Materials, an Office of Science user facility, is supported by the U.S. Department of Energy, Office of Science, Office of Basic Energy Sciences, under Contract No. DE-AC02-06CH11357. L.J. acknowledges support from the ARO (W911NF-18-1-0020, W911NF-18-1-0212), ARO MURI (W911NF-16-1-0349), AFOSR MURI (FA9550-15-1-0015, FA9550-19-1-0399), NSF (EFMA-1640959, OMA-1936118, EEC-1941583), NTT Research, and the Packard Foundation (2013-39273). The authors thank David Czaplewski, Ralu Divan, Liliana Stan, and Suzanne Miller for helping with the device fabrication.

APPENDIX A: LATERAL CONFINEMENT OF HBAR PHONONS

Our YIG/GGG device has a thickness of $527 \mu\text{m}$, and the lateral dimension of the YIG film is 800 to $900 \mu\text{m}$. These dimensions determine (and can actually be roughly considered as) the spatial extension of the HBAR phonons along both the out-of-plane (z) and in-plane (x and y) directions. Although these dimensions are comparable, it is worth noting that the wavelengths are completely different along both directions. Along the out-of-plane direction, the high-overtone phonons have a wavelength of around 400 nm (determined roughly as twice the YIG film thickness), while along the in-plane direction the wavelength is around 4000 times longer (approximated as twice the YIG lateral dimensions for the low-order standing waves along that direction). Therefore the wave vectors of the HBAR phonons are mainly along the z direction, with a negligibly small component along the in-plane directions. As a result, we can ignore the effect of the lateral confinement and assume uniform mode distribution along lateral

directions for simplicity when analyzing phonon properties such as FSR.

APPENDIX B: LONGITUDINAL ACOUSTIC PHONONS

On the YIG/GGG device, the high-overtone phonon resonances can be formed by either transverse acoustic waves or longitudinal acoustic waves. Although they can coexist in the same frequency range, the longitudinal modes can be easily distinguished from the transverse HBAR phonons because of their distinctively different FSR. Similar to the transverse HBAR phonons, the FSR for the longitudinal HBAR phonons can be calculated as $\Delta f_{\text{LA}} = c_p/2d = 6.01$ MHz, where $c_p = \sqrt{E(1-\nu)/\rho(1+\nu)(1-2\nu)} = 6331$ m/s is the propagation speed of the longitudinal elastic waves in GGG. Clearly this FSR is much larger than that of the transverse acoustic phonons, making it possible to identify the longitudinal phonons from the measured spectrum.

However, in our experiment such longitudinal phonon modes are not observed. This can be explained by their vanished coupling strength with the magnon mode. Following Eq. (17) in Ref. [57] that leads to our Eq. (3), and keeping only the first-order terms, the magnetoelastic energy for the longitudinal acoustic phonons can be obtained as

$$U_{\text{ME}}^{\text{LA}} = \frac{2B_2}{M_s} (m_x \bar{\epsilon}_{xz} + m_y \bar{\epsilon}_{yz}),$$

where $\bar{\epsilon}_{xz} = \frac{1}{2} (\partial u_x / \partial z + \partial u_z / \partial x)$ and $\bar{\epsilon}_{yz} = \frac{1}{2} (\partial u_y / \partial z + \partial u_z / \partial y)$. Ideal longitudinal phonons have displacements only along the z direction ($u_z \neq 0$) while the in-plane displacements are all zero ($u_x = u_y = 0$, and accordingly, $\partial u_x / \partial z = \partial u_y / \partial z = 0$). In addition, since the phonon distribution can be considered as nearly uniform along lateral directions, we have $\partial u_z / \partial x = \partial u_z / \partial y = 0$. As a result, $U_{\text{ME}}^{\text{LA}} = 0$, leading to a vanished coupling strength ($g_{mb}^{\text{LA}} \propto \int U_{\text{ME}}^{\text{LA}} dV = 0$) between magnons and longitudinal phonons.

-
- [1] H. Huebl, C. Zollitsch, J. Lotze, F. Hocke, M. Greifenstein, A. Marx, R. Gross, and S. Goennenwein, High Cooperativity in Coupled Microwave Resonator Ferrimagnetic Insulator Hybrids, *Phys. Rev. Lett.* **111**, 127003 (2013).
- [2] X. Zhang, C.-L. Zou, L. Jiang, and H. X. Tang, Strongly Coupled Magnons and Cavity Microwave Photons, *Phys. Rev. Lett.* **113**, 156401 (2014).
- [3] Y. Tabuchi, S. Ishino, T. Ishikawa, R. Yamazaki, K. Usami, and Y. Nakamura, Hybridizing Ferromagnetic Magnons and Microwave Photons in the Quantum Limit, *Phys. Rev. Lett.* **113**, 083603 (2014).
- [4] L. Bai, M. Harder, Y. P. Chen, X. Fan, J. Q. Xiao, and C.-M. Hu, Spin Pumping in Electrostatically Coupled Magnon-Photon Systems, *Phys. Rev. Lett.* **114**, 227201 (2015).
- [5] M. Goryachev, W. G. Farr, D. L. Creedon, Y. Fan, M. Kostylev, and M. E. Tobar, High-Cooperativity Cavity QED with Magnons at Microwave Frequencies, *Phys. Rev. Appl.* **2**, 054002 (2014).
- [6] X. Zhang, N. Zhu, C.-L. Zou, and H. X. Tang, Optomagnonic Whispering Gallery Microresonators, *Phys. Rev. Lett.* **117**, 123605 (2016).
- [7] A. Osada, R. Hisatomi, A. Noguchi, Y. Tabuchi, R. Yamazaki, K. Usami, M. Sadgrove, R. Yalla, M. Nomura, and Y. Nakamura, Cavity Optomagnonics with Spin-Orbit Coupled Photons, *Phys. Rev. Lett.* **116**, 223601 (2016).
- [8] J. A. Haigh, A. Nunnenkamp, A. J. Ramsay, and A. J. Ferguson, Triple-Resonant Brillouin Light Scattering in Magneto-Optical Cavities, *Phys. Rev. Lett.* **117**, 133602 (2016).
- [9] X. Zhang, C.-L. Zou, L. Jiang, and H. X. Tang, Cavity magnomechanics, *Sci. Adv.* **2**, e1501286 (2016).
- [10] Y.-P. Wang, J. W. Rao, Y. Yang, P.-C. Xu, Y. S. Gui, B. M. Yao, J. Q. You, and C.-M. Hu, Nonreciprocity and Unidirectional Invisibility in Cavity Magnonics, *Phys. Rev. Lett.* **123**, 127202 (2019).
- [11] X. Zhang, A. Galda, X. Han, D. Jin, and V. M. Vinokur, Broadband Nonreciprocity Enabled by Strong Coupling of Magnons and Microwave Photons, *Phys. Rev. Appl.* **13**, 044039 (2020).
- [12] N. Zhu, X. Han, C.-L. Zou, M. Xu, and H. X. Tang, Magnon-photon strong coupling for tunable microwave circulators, *Phys. Rev. A* **101**, 043842 (2020).
- [13] D. Zhang, X.-Q. Luo, Y.-P. Wang, T.-F. Li, and J. Q. You, Observation of the exceptional point in cavity magnon-polaritons, *Nat. Commun.* **8**, 1368 (2017).
- [14] M. Harder, L. Bai, P. Hyde, and C.-M. Hu, Topological properties of a coupled spin-photon system induced by damping, *Phys. Rev. B* **95**, 214411 (2017).
- [15] X. Zhang, K. Ding, X. Zhou, J. Xu, and D. Jin, Experimental Observation of an Exceptional Surface in Synthetic Dimensions with Magnon Polaritons, *Phys. Rev. Lett.* **123**, 237202 (2019).
- [16] R. Hisatomi, A. Osada, Y. Tabuchi, T. Ishikawa, A. Noguchi, R. Yamazaki, K. Usami, and Y. Nakamura, Bidirectional conversion between microwave and light via ferromagnetic magnons, *Phys. Rev. B* **93**, 174427 (2016).
- [17] N. Zhu, X. Zhang, X. Han, C. L. Zou, C. Zhong, C. H. Wang, L. Jiang, and H. X. Tang, Waveguide cavity optomagnonics for broadband multimode microwave-to-optics conversion, *Optica* **7**, 1291 (2020).
- [18] G. Flower, J. Bourhill, M. Goryachev, and M. E. Tobar, Broadening frequency range of a ferromagnetic axion haloscope with strongly coupled cavity-magnon polaritons, *Phys. Dark Universe* **25**, 100306 (2019).
- [19] T. Trickle, Z. Zhang, and K. M. Zurek, Detecting Light Dark Matter with Magnons, *Phys. Rev. Lett.* **124**, 201801 (2020).
- [20] Y. Tabuchi, S. Ishino, A. Noguchi, T. Ishikawa, R. Yamazaki, K. Usami, and Y. Nakamura, Coherent coupling between a ferromagnetic magnon and a superconducting qubit, *Science* **349**, 405 (2015).
- [21] D. Lachance-Quirion, S. Piotr Wolski, Y. Tabuchi, S. Kono, K. Usami, and Y. Nakamura, Entanglement-based

- single-shot detection of a single magnon with a superconducting qubit, *Science* **367**, 425 (2020).
- [22] S. P. Wolski, D. Lachance-Quirion, Y. Tabuchi, S. Kono, A. Noguchi, K. Usami, and Y. Nakamura, Dissipation-Based Quantum Sensing of Magnons with a Superconducting Qubit, *Phys. Rev. Lett.* **125**, 117701 (2020).
- [23] M. Li, W. H. P. Pernice, C. Xiong, T. Baehr-Jones, M. Hochberg, and H. X. Tang, Harnessing optical forces in integrated photonic circuits, *Nature* **456**, 480 (2008).
- [24] S. Weis, R. Riviere, S. Deleglise, E. Gavartin, O. Arcizet, A. Schliesser, and T. J. Kippenberg, Optomechanically induced transparency, *Science* **330**, 1520 (2010).
- [25] J. D. Teufel, T. Donner, D. Li, J. W. Harlow, M. S. Allman, K. Cicak, A. J. Sirois, J. D. Whittaker, K. W. Lehnert, and R. W. Simmonds, Sideband cooling of micromechanical motion to the quantum ground state, *Nature* **475**, 359 (2011).
- [26] J. Chan, T. P. Mayer Alegre, A. H. Safavi-Naeini, J. T. Hill, A. Krause, S. Groblacher, M. Aspelmeyer, and O. Painter, Laser cooling of a nanomechanical oscillator into its quantum ground state, *Nature* **478**, 89 (2011).
- [27] C. Kittel, Interaction of spin waves and ultrasonic waves in ferromagnetic crystals, *Phys. Rev.* **110**, 836 (1958).
- [28] Ernst Schlomann, Generation of phonons in high-power ferromagnetic resonance experiments, *J. Appl. Phys.* **31**, 1647 (1960).
- [29] J. R. Eshbach, Spin-wave propagation and the magnetoelastic interaction in yttrium iron garnet, *J. Appl. Phys.* **34**, 1298 (1963).
- [30] E. Schlomann and R. I. Joseph, Generation of spin waves in nonuniform magnetic fields. III. Magnetoelastic interaction, *J. Appl. Phys.* **35**, 2382 (1964).
- [31] R. W. Damon and H. van de Vaart, Dispersion of spin waves and magnetoelastic waves in YIG, *Proc. IEEE* **53**, 348 (1965).
- [32] B. A. Auld, J. H. Collins, and H. R. Zapp, Adiabatic time domain conversion of hybrid magnetoelastic waves in YIG, *Appl. Phys. Lett.* **10**, 186 (1967).
- [33] R. L. Comstock and N. Kusnezov, Magnetoelastic-elastic wave scattering, *J. Appl. Phys.* **38**, 3740 (1967).
- [34] S. M. Rezende and F. R. Morgenthaler, Magnetoelastic waves in time-varying magnetic fields. I. Theory, *J. Appl. Phys.* **40**, 524 (1969).
- [35] T. Yukawa and K. Abe, FMR spectrum of magnetostatic waves in a normally magnetized YIG disk, *J. Appl. Phys.* **45**, 3146 (1974).
- [36] R. E. Camley, Magnetoelastic waves in a ferromagnetic film on a nonmagnetic substrate, *J. Appl. Phys.* **50**, 5272 (1979).
- [37] G. Komoriya and G. Thomas, Magnetoelastic-surface waves on YIG substrate, *J. Appl. Phys.* **50**, 6459 (1979).
- [38] B. D. Zaitsev, A. V. Ermolenko, and V. A. Fedorenko, Magnetoacoustic SAW interaction in YIG films, *EEE Trans. Ultrason. Ferroelectr. Freq. Control* **45**, 356 (1998).
- [39] Yu A. Filimonova, G. T. Kazakova, Yu V. Khivintseva, I. M. Kotelaynskiib, and A. V. Maryachinc, Nonlinear properties of magnetoelastic Rayleigh waves in ferrite films, *J. Magn. and Magn. Mater.* **272**, 1009 (2004).
- [40] D. A. Bozhko, P. Clausen, G. A. Melkov, V. S. L'vov, A. Pomyalov, V. I. Vasyuchka, A. V. Chumak, B. Hillebrands, and A. A. Serga, Bottleneck Accumulation of Hybrid Magnetoelastic Bosons, *Phys. Rev. Lett.* **118**, 237201 (2017).
- [41] I. Lisenkov, A. Jander, and P. Dhagat, Magnetoelastic parametric instabilities of localized spin waves induced by traveling elastic waves, *Phys. Rev. B* **99**, 184433 (2019).
- [42] R. Verba, V. Tiberkevich, and A. Slavin, Wide-Band Nonreciprocity of Surface Acoustic Waves Induced by Magnetoelastic Coupling with a Synthetic Antiferromagnet, *Phys. Rev. Appl.* **12**, 054061 (2019).
- [43] P. J. Shah, D. A. Bas, I. Lisenkov, A. Matyushov, N. X. Sun, and M. R. Page, Giant nonreciprocity of surface acoustic waves enabled by the magnetoelastic interaction, *Sci. Adv.* **6**, eabc5648 (2020).
- [44] M.-S. Ding, L. Zheng, and C. Li, Ground-state cooling of a magnomechanical resonator induced by magnetic damping, *J. Opt. Soc. Am. B* **37**, 627 (2020).
- [45] J. Li and S.-Y. Zhu, Entangling two magnon modes via magnetostrictive interaction, *New J. Phys.* **21**, 085001 (2019).
- [46] X. Zhang, G. E. W. Bauer, and T. Yu, Unidirectional Pumping of Phonons by Magnetization Dynamics, *Phys. Rev. Lett.* **125**, 077203 (2020).
- [47] M. Xu, K. Yamamoto, J. Puebla, K. Baumgaertl, B. Rana, K. Miura, H. Takahashi, D. Grundler, S. Maekawa, and Y. Otani, Nonreciprocal surface acoustic wave propagation via magneto-rotation coupling, *Sci. Adv.* **6**, eabb1724 (2020).
- [48] C. L. Ordóñez-Romero, O. V. Kolokoltsev, N. Qureshi V. Grimalsky, and R. Ortega, Observation of indirect parallel pumping of magneto-elastic modes in layered YIG/GGG structures, *Solid State Commun.* **141**, 33 (2007).
- [49] N. I. Polzikova, S. G. Alekseev, I. I. Pyataikin, I. M. Kotelyanskii, V. A. Luzanov, and A. P. Orlov, Acoustic spin pumping in magnetolectric bulk acoustic wave resonator, *AIP Adv.* **6**, 056306 (2016).
- [50] P. Chowdhury, A. Jander, and P. Dhagat, Nondegenerate parametric pumping of spin waves by acoustic waves, *IEEE Magn. Lett.* **8**, 3108204 (2017).
- [51] K. An, A. N. Litvinenko, R. Kohno, A. A. Fuad, V. V. Naleto, L. Vila, U. Ebels, G. de Loubens, H. Hurdequint, N. Beaulieu, J. Ben Youssef, N. Vukadinovic, G. E. W. Bauer, A. N. Slavin, V. S. Tiberkevich, and O. Klein, Coherent long-range transfer of angular momentum between magnon Kittel modes by phonons, *Phys. Rev. B* **101**, 060407(R) (2020).
- [52] F. Vanderveken, F. Ciubotaru, and C. Adelman, Magnetoelastic waves in thin films, [arXiv:2003.12099](https://arxiv.org/abs/2003.12099) (2020).
- [53] <https://www.rogerscorp.com/>.
- [54] M. Ye and H. Dotsch, Magnetoelastic instabilities in the ferromagnetic resonance of magnetic garnet films, *Phys. Rev. B* **44**, 9458 (1991).
- [55] N. S. Sokolov, V. V. Fedorov, A. M. Korovin, S. M. Sutorin, D. A. Baranov, S. V. Gastev, B. B. Krichevstov, K. Yu Maksimova, A. I. Grunin, V. E. Bursian, L. V. Lutsev, and M. Tabuchi, Thin yttrium iron garnet films grown by pulsed laser deposition: Crystal structure, static, and dynamic magnetic properties, *J. Appl. Phys.* **119**, 023903 (2016).
- [56] V. V. Vitko, A. A. Nikitin, A. V. Kondrashov, A. A. Nikitin, A. B. Ustinov, P. Yu Belyavskiy, B. A. Kalinikos, and J. E. Butler, Microwave filter based on Lamb modes for

- optoelectronic generator, *J. Phys.: Conf. Ser.* **661**, 012049 (2015).
- [57] C. Gonzalez-Ballester, D. Hummer, J. Gieseler, and O. Romero-Isart, Theory of quantum acoustomagnonics and acoustomechanics with a micromagnet, *Phys. Rev. B* **101**, 125404 (2020).
- [58] I. S. Maksymov and M. Kostylev, Broadband stripline ferromagnetic resonance spectroscopy of ferromagnetic films, multilayers and nanostructures, *Physica E* **69**, 253 (2015).
- [59] Y. K. Fetisov and C. E. Patton, Thermal microwave foldover and bistability in ferromagnetic resonance, *IEEE T. Magn* **40**, 473 (2004).
- [60] P. Hyde, B. M. Yao, Y. S. Gui, Guo-Qiang Zhang, J. Q. You, and C.-M. Hu, Direct measurement of foldover in cavity magnon-polariton systems, *Phys. Rev. B* **98**, 174423 (2018).
- [61] N. Timoney, B. Lauritzen, I. Usmani, M. Afzelius, and N. Gisin, Atomic frequency comb memory with spin-wave storage in $153\text{Eu}^{3+}:\text{Y}_2\text{SiO}_5$, *J. Phys. B: At. Mol. Opt. Phys.* **45**, 124001 (2012).
- [62] M. Gundogan, M. Mazzera, P. M. Ledingham, M. Cristiani, and H. de Riedmatten, Coherent storage of temporally multimode light using a spin-wave atomic frequency comb memory, *New J. Phys* **15**, 045012 (2013).
- [63] Xufeng Zhang, Chang-Ling Zou, Na Zhu, Florian Marquardt, Liang Jiang, and Hong X. Tang, Magnon dark modes and gradient memory, *Nat. Commun.* **6**, 8914 (2015).